Ceramics International xxx (xxxx) xxx

Contents lists available at ScienceDirect

Ceramics International

journal homepage: www.elsevier.com/locate/ceramint

Crystal structure, infrared-reflectivity spectra, and microwave dielectric properties of novel $Ce_2(MoO_4)_2(Mo_2O_7)$ ceramics

Huanrong Tian [a], Lintao Liu [a], Jialun Du [b], Haitao Wu [a,*], MingLing Li [c,**], Bingjing Tao [d]

[a] School of Environmental and Material Engineering, Yantai University, Yantai, 264005, Shandong, China
[b] Colleges of Humanities of Yantai University, Yantai University, Yantai, 264005, Shandong, China
[c] Engineering Technology Research Center of Preparation and Application of Industrial Ceramics of AnHui Province, Chaohu University, Chaohu, 238024, China
[d] School of Materials Science and Engineering, University of Jinan, Jinan, 250022, Shandong, China

ARTICLE INFO

Keywords:
$Ce_2(MoO_4)_2(Mo_2O_7)$
Chemical bond theory
Infrared-reflectivity spectra
Microwave dielectric ceramic

ABSTRACT

Novel $Ce_2(MoO_4)_2(Mo_2O_7)$ (CMO) ceramics were prepared by a conventional solid-state method, and the microwave dielectric properties were investigated. X-ray diffraction results illustrated that pure $Ce_2(MoO_4)_2(Mo_2O_7)$ structure formed upon sintering at 600 °C-725 °C. [CeO_7], [CeO_8], [MoO_4], and [MoO_6] polyhedra were connected to form a three-dimensional structure of CMO ceramics. Analysis based on chemical bond theory indicated that the Mo–O bond critically affected the ceramics' performance. Furthermore, infrared-reflectivity spectra analysis revealed that the primary polarisation contribution was from ionic polarisation. Notably, the optimum microwave dielectric properties of $\varepsilon_r = 10.69$, $Q{\cdot}f = 49{,}440$ GHz (@ 9.29 GHz), and $\tau_f = -30.4$ ppm/°C were obtained in CMO ceramics sintered at 700 °C.

1. Introduction

Microwave dielectric ceramics, as key materials in modern telecommunication, are in various components, such as antennas, filters, and capacitors [1–3]. Nowadays, the carrier frequency of 5G is extended to millimeter wave band rather than microwave band. Thus, higher requirements for the performance of microwave dielectric ceramics are brought forward: a low permittivity (ε_r) to avoid the signal delay, a high quality factor ($Q{\cdot}f$) for better selectivity at higher frequencies and a near-zero temperature coefficient of resonant frequency (τ_f) for the frequency stability [4,5]. Moreover, a low sintering temperature (usually <960 °C) is the engineering requirement of densified ceramics to achieve high-integration fabrication. According to Sebastian et al. [6], molybdenum oxide-based ceramics are appropriate candidates for integration because of their ultra-low sintering temperature and potential use in adjustable comprehensive dielectric properties.

Recently, many molybdenum oxide-based ceramics have been reported. For instance, a series of tetragonal scheelite-structured $XMoO_4$ ceramics with ε_r values of 10–35, $Q{\cdot}f$ values below 70,000 GHz, and varied temperature stability have been investigated [7,8]. Trigonal-structured $Ln_2Zr_3(MoO_4)_9$ ceramics with basic performances of $\varepsilon_r = 10$–11, $Q{\cdot}f = 20{,}000$–80,000 GHz, and negative τ_f values have been systematically reported by our group [9–11]. The substitution of an element at a specific position results in the microadjustment of bonding characteristics and crystal structure, playing a significant role in the variation of properties [12,13]. Furthermore, the Ag_2O_3–MoO_3 system with different phases such as $Ag_2Mo_2O_7$, Ag_2MoO_4 and $Ag_2Mo_4O_{13}$ has been reported. It possesses ultra-low sintering temperature (<500 °C), meeting the co-fired metal of Ag and with chemical compatibility. Nevertheless, these candidates present high dielectric loss and poor thermal stability [14]. These findings show that molybdenum oxide-based ceramics have a low crystal-growth temperature. The crystal structure, phase composition, and internal bond characteristics of the ceramics jointly affect their dielectric properties. Therefore, the development of novel molybdenum oxide-based ceramics has scientific importance for future practical applications.

$Ce_2(MoO_4)_2(Mo_2O_7)$ material belongs to the triclinic system with the space group of $P\bar{1}(2)$. It was firstly identified in 1982 after calcining a mixture of CeO_2 and MoO_3 at 700 °C for 24 h [15]. However, few reports have focused on the feasibility of this material in practical applications. Considering the lower sintering temperature, higher crystallinity, and similar chemical composition compared with traditional molybdenum oxide-based ceramics, $Ce_2(MoO_4)_2(Mo_2O_7)$ was refabricated in the

* Corresponding author.
** Corresponding author.
E-mail addresses: wuhaitao@ytu.edu.cn (H. Wu), 053014@chu.edu.cn (M. Li).

https://doi.org/10.1016/j.ceramint.2021.08.011
Received 7 June 2021; Received in revised form 22 July 2021; Accepted 2 August 2021
Available online 10 August 2021

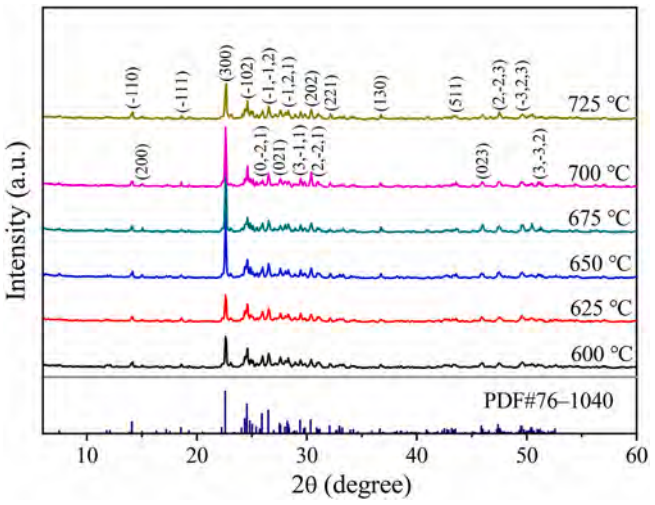

Fig. 1. X-ray diffraction patterns of $Ce_2(MoO_4)_2(Mo_2O_7)$ ceramics sintered at different temperatures (vertical lines correspond to JCPDS pattern no. 76–1040).

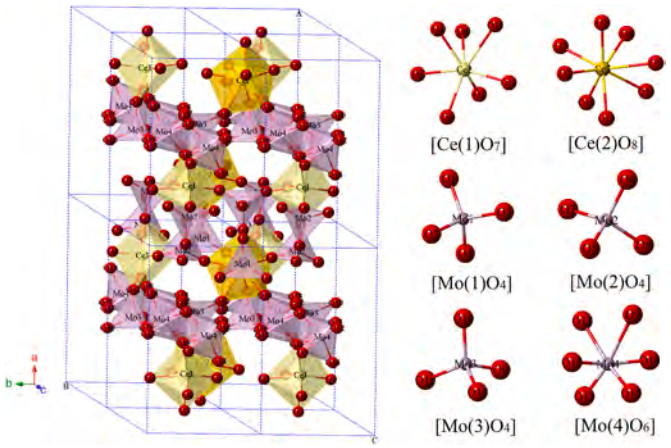

Fig. 2. Schematic crystal structure of $Ce_2(MoO_4)_2(Mo_2O_7)$ ceramics.

current work to investigate its feasibility in microwave dielectric applications. Chemical bond theory and spectral analysis were adapted for the first time to assist the research on the structure–property relationship.

2. Experimental procedure

To fabricate the ceramics for further investigation, $Ce_2(MoO_4)_2(Mo_2O_7)$ was initially synthesised using the traditional solid-state method. High-purity oxide powders of CeO_2 (99.9%, Macklin) and MoO_3 (99.95%, Aladdin) were weighed at 1:2 mol ratio and ball milled with anhydrous ethanol for 24 h in a polyethylene bottle. The mixture slurry was dried in an oven to obtain raw powders and then calcined in a muffle furnace at 650 °C for 2 h, which was less than one-tenth of the treatment time reported in a previous study [15]. Thereafter, the pre-crystallised powders were remixed for 24 h, dried, and combined with 10 wt% high-purity paraffin as the binder. The resultant powders were pressed into green pellets with a diameter of 10 mm and a height of 6 mm under 6 MPa. All pristine pellets had paraffin removed and were finally sintered at 600 °C-725 °C for characterisation and dielectric measurement.

The phase composition and crystal structure of the ceramics at different temperatures were investigated with a Rigaku diffractometer using CuKα radiation. The morphology on the CMO surface was obtained by scanning electron microscopy. A Bruker IFS 66v FTIR spectrometer was used to obtain the infrared-reflectivity spectra (IRRS) information. The Raman spectra was collected at 30–2500 cm^{-1} by using LabRAM HR Evolution. The apparent density of specimens was measured and calculated based on the Archimedes principle. ε_r and $Q{\cdot}f$ of the CMO ceramics were obtained using the Hakki–Coleman dielectric resonator methodology with a network analyser (Agilent 5234A) [16, 17]. According to $\tau_f = \Delta f/(f_{25}\Delta T)$, τ_f was acquired by the temperature chamber at 25 °C-85 °C.

3. Results and discussion

Fig. 1 exhibits the X-ray diffraction patterns of CMO ceramics sintered at different temperatures. All samples presented similar patterns, which well matched the JCPDS card of 76–1040 belonging to the $Ce_2(MoO_4)_2(Mo_2O_7)$ structure with the $P\bar{1}(2)$ space group. No diffraction peaks that identified second phases were observed, demonstrating that the current fabrication process provided sufficient sintering driving force for pure CMO samples. The intensity of the (300) diffraction peak located at around 22.6° presented an increased tendency with increased temperature from 600 °C to 700 °C, indicating that the preferential grain grew on the (300) plane of CMO ceramic. However, the decrease in the (300) peak and SNR throughout the entire pattern at 725 °C indicated the appearance of an amorphous phase. To explore the crystal structure of CMO samples, a series of Rietveld refinement was conducted, and the refined cell parameters, lattice volume, and confidence parameters are presented in Table 1. Under a reasonable degree of confidence, no apparent changes occurred in cell volume with a variation amount less than 0.09%, demonstrating the stability of the CMO phase between 600 °C-725 °C.

Fig. 2 illustrates the crystal structure of CMO ceramics comprising $[CeO_7]$, $[CeO_8]$, $[MoO_4]$, and $[MoO_6]$ polyhedra. Two Ce atoms were in different distorted environments, and the Ce(1) and Ce(2) atoms were seven- and eight-coordination, respectively. The four crystallographically different Mo atoms in the cell structure, Mo(1), Mo(2), and Mo(3) atoms, surrounded by four O atoms formed into a tetrahedral

Table 1
Refined cell parameters, lattice volume, and confidence parameters of $Ce_2(MoO_4)_2(Mo_2O_7)$ ceramics.

Structural parameters	Sintering temperature (°C)					
	600	625	650	675	700	725
a (Å)	11.8861	11.8828	11.8891	11.8921	11.8931	11.8900
b (Å)	7.4948	7.4959	7.4966	7.5003	7.5012	7.4984
c (Å)	7.3866	7.3827	7.3831	7.3808	7.3776	7.3804
α (°)	94.3401	94.3047	94.3405	94.3474	94.3406	94.3307
β (°)	97.3555	97.3307	97.4004	97.3820	97.4053	97.3990
γ (°)	88.5771	88.5988	88.5783	88.6058	88.5741	88.5885
V_m (Å^3)	650.67	650.31	650.61	650.91	650.74	650.59
R_p (%)	9.02	9.28	10.6	13.0	13.2	11.0
R_{wp} (%)	11.8	11.8	13.9	17.3	17.3	14.2
χ^2	2.16	2.01	2.95	4.18	4.27	2.93

Table 2
Atom position and occupancy of $Ce_2(MoO_4)_2(Mo_2O_7)$ ceramics.

Atom	Wyckoff position	Site	x	y	z	Occupancy
Ce1	2*i*	1	0.2235	0.3977	0.2732	1.0000
Ce2	2*i*	1	0.7772	0.9028	0.1805	1.0000
Mo1	2*i*	1	0.1284	0.9203	0.2727	1.0000
Mo2	2*i*	1	0.8734	0.4238	0.2193	1.0000
Mo3	2*i*	1	0.5259	0.2480	0.0684	1.0000
Mo4	2*i*	1	0.5289	0.6720	0.4044	1.0000
O1	2*i*	1	−0.0161	0.8938	0.2027	1.0000
O2	2*i*	1	0.1503	1.0074	0.5013	1.0000
O3	2*i*	1	0.1965	0.7114	0.2474	1.0000
O4	2*i*	1	0.1859	1.0846	0.1439	1.0000
O5	2*i*	1	1.0186	0.3945	0.2162	1.0000
O6	2*i*	1	0.8491	0.5099	0.4381	1.0000
O7	2*i*	1	0.8102	0.2153	0.1607	1.0000
O8	2*i*	1	0.8192	0.5893	0.0633	1.0000
O9	2*i*	1	0.5874	0.4264	0.2042	1.0000
O10	2*i*	1	0.5922	0.0469	0.1331	1.0000
O11	2*i*	1	0.3797	0.2570	0.0845	1.0000
O12	2*i*	1	0.5512	0.2826	−0.1656	1.0000
O13	2*i*	1	0.4675	0.8327	0.5307	1.0000
O14	2*i*	1	0.6624	0.7605	0.3850	1.0000
O15	2*i*	1	0.5937	0.5187	0.5877	1.0000

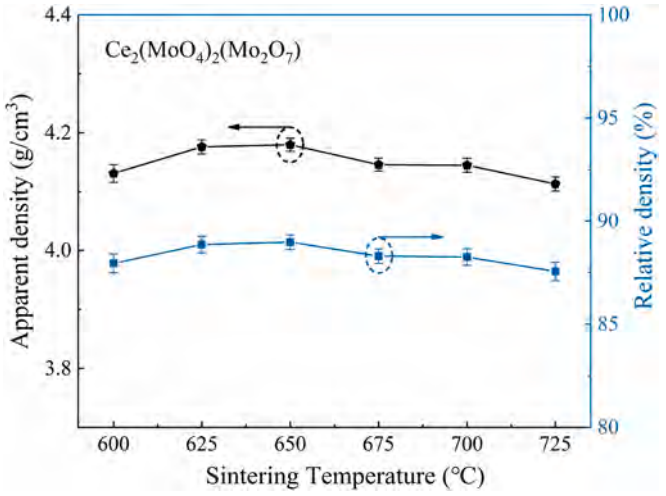

Fig. 3. Apparent and relative density of $Ce_2(MoO_4)_2(Mo_2O_7)$ ceramics as a function of sintering temperature.

coordination, whereas the Mo(4) atoms were linked to six O atoms within a distorted octahedral coordination. Two neighbouring [Mo(4)O_6] tetrahedra shared their edge to form a Mo_2O_{10} unit, which was connected by [Mo(1)O_4] through corner sharing, forming a Mo_4O_{14} chain. The Mo_4O_{14} chains were vertically connected to the chain direction into a three-dimensional structure through the [Mo(2)O_4] and [Mo(3)O_4] tetrahedra and the [Ce(1)O_7] and [Ce(2)O_8] polyhedra sharing edges and corners [18]. Besides, the atom position and occupancy are listed in Table 2, and the Ce, Mo, and O atoms occupied the 2*i* Wyckoff position.

The apparent and relative density of the CMO ceramics sintered at different temperatures is exhibited in Fig. 3. Relative density was calculated using the following equations.

$$\rho_{th.} = \frac{ZM}{N_A V_m} \quad (1)$$

$$\rho_{re.} = \frac{\rho_{ap.}}{\rho_{th.}} \times 100\% \quad (2)$$

where Z is 2 and is the number of molecules, M is 919.98 g/mol and is

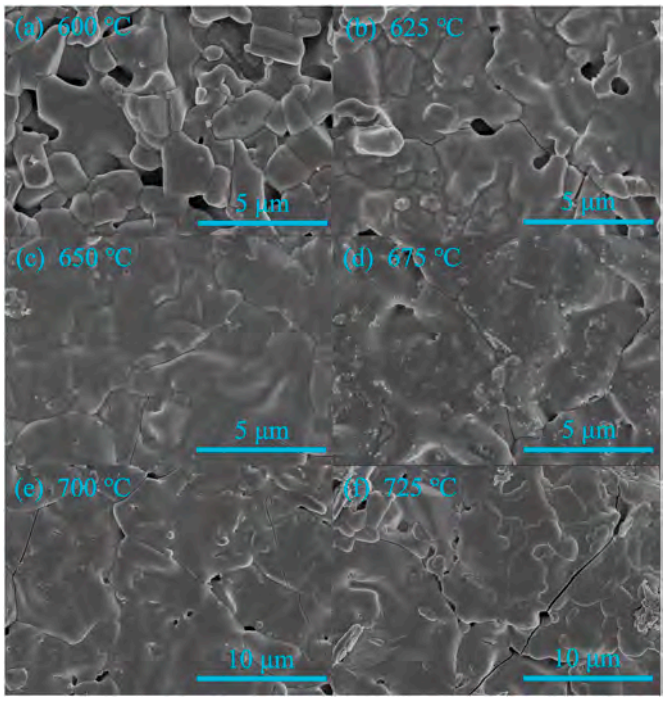

Fig. 4. Morphologies on the surface of $Ce_2(MoO_4)_2(Mo_2O_7)$ ceramics sintered at (a) 600 °C, (b) 625 °C, (c) 650 °C, (d) 675 °C, (e) 700 °C, and (f) 725 °C.

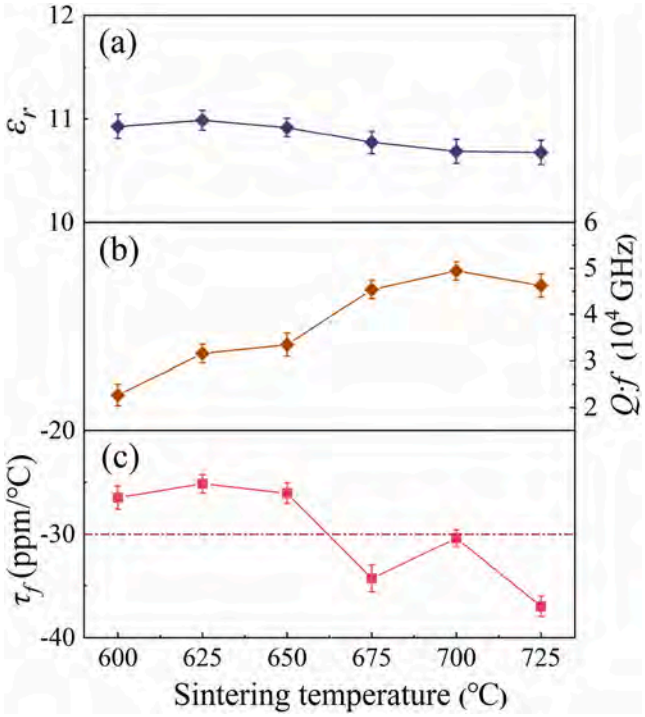

Fig. 5. Variations in (a) permittivity (ε_r), (b) quality factor ($Q{\cdot}f$), and (c) temperature coefficient of resonant frequency (τ_f) of $Ce_2(MoO_4)_2(Mo_2O_7)$ ceramics as a function of sintering temperature.

the theoretical molecular weight. N_A is the Avogadro's constant, and V_m is the refined unit-cell volume obtained from Table 1. With increased temperature from 600 °C to 650 °C, relative density slightly increased from 87.94% to 88.97%, which was attributed to the elimination of pores. Thereafter, density decreased and finally reached 87.56%, which may be primarily due to the blocked pores caused by the existence of the

amorphous phase. To verify the above speculation, the morphologies on the surface of CMO ceramics were determined, and results are listed in Fig. 4(a)–4(f). At 600 °C and 625 °C, notable intergranular pores corresponding to the lower density were observed, as shown in Fig. 3. Thereafter, all samples were relatively densified, as shown in Fig. 4(c)–4(e). Notably, microcracks and a glass phase could be observed in Fig. 4(f), which are usually considered to be the main factors affecting density reduction. In addition, a significant increase in grain size was observed in Figs. 3(a)–4(e), while the grain size in Fig. 3(f) decreased due to the appearance of fine grains.

Fig. 5 presents the variation in microwave dielectric properties of CMO ceramics sintered at different temperatures. ε_r slightly increased from 10.93 to 10.99 with increased temperature from 600 °C to 625 °C and then slightly decreased with further increased sintering temperature. This finding was consistent with the variation in relative density, indicating that the ε_r value was related to the density of CMO ceramics. Furthermore, ε_r is associated with polarisability [19–21], and the theoretical dielectric polarisability ($\alpha_{theo.}$) could be calculated by Shannon's addition rule [22].

$$\alpha_{theo.} = \alpha(Ce_2(MoO_4)_2(Mo_2O_7)) = 2\alpha\left(Ce^{3+}\right) + 4\alpha\left(Mo^{6+}\right) + 15\alpha\left(O^{2-}\right) \quad (3)$$

where $\alpha(Ce^{3+}) = 6.15$ Å^3, $\alpha(Mo^{6+}) = 3.28$ Å^3, $\alpha(O^{2-}) = 2.01$ Å^3. In addition, the observed dielectric polarisability ($\alpha_{obs.}$) could be expressed as follows:

$$\alpha_{obs.} = \frac{1}{b} V_m \frac{\varepsilon - 1}{\varepsilon + 2} \quad (4)$$

where ε and V_m are the measured permittivity and refined cell volume, respectively. b is a constant value ($4\pi/3$). $\alpha_{obs.}$ was calculated to be 59.31, which approached $\alpha_{theo.}$ (55.57). Fig. 5(b) also exhibits the change in $Q{\cdot}f$ value, which initially increased from 22,689 GHz at 600 °C to 49,440 GHz at 700 °C and then slightly decreased to 46,256 GHz at 725 °C. $Q{\cdot}f$ is generally susceptible to extrinsic (phase composition, porosity, and grain size) and intrinsic (lattice vibration) losses [23–25]. The single phase formed throughout the sintering range. Hence, the increase of $Q{\cdot}f$ values could be attributed to increased grain size and reduced pore [26], whereas the decrease was related to the appearance of microcracks and fine grain size [27,28]. The τ_f values were stable at about −30 ppm/°C (Fig. 5(c)), which presented less dependence on sintering temperature. Furthermore, the τ_f value needs to be further adjusted by compensator (e.g. TiO_2) for practical application. Notably, the desirable microwave dielectric properties ($\varepsilon_r = 10.69$, $Q{\cdot}f = 49{,}440$ GHz (@ 9.29 GHz), and $\tau_f = -30.4$ ppm/°C) of CMO ceramics could be obtained upon sintering at 700 °C.

To further discuss the inherent connection between properties and structure, chemical bond theory was used to investigate CMO ceramics. Zhang et al. [29] succeeded in generalizing P–V–L theory for multibond systems and gave an explicit expression about how to decompose the complex crystals into binary crystals. Suppose that A denotes cations and B anions, any multiband complex crystal could be written as:

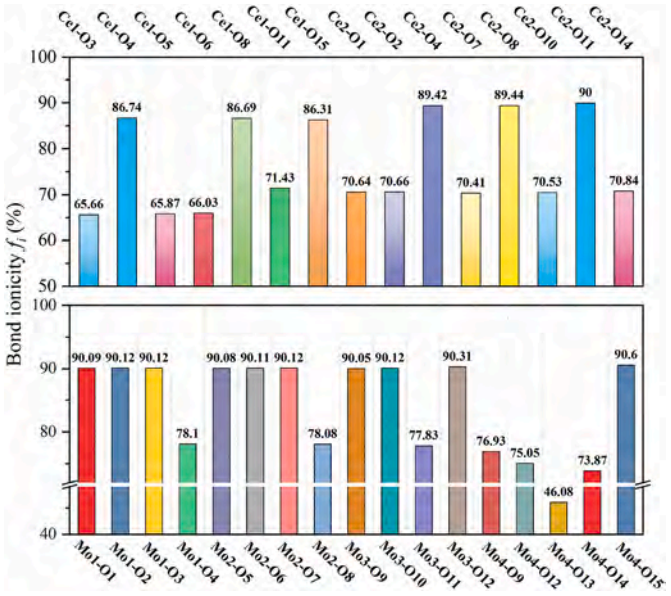

Fig. 6. Bond ionicity (f_i) of each bond for $Ce_2(MoO_4)_2(Mo_2O_7)$ ceramics.

$$A^1_{a1}A^2_{a2}\ldots A^i_{ai}\ldots B^1_{b1}B^2_{b2}\ldots B^j_{bj} \quad (5)$$

where A^i and B^j represent the different elements or the different sites of a given element of cations and anions, respectively. a_i and b_j represent the number of corresponding elements. Any complex crystals could be decomposed into the sum of binary crystals with the crystallographic data using the following formula:

$$A^1_{a1}A^2_{a2}\ldots A^i_{ai}\ldots B^1_{b1}B^2_{b2}\ldots B^j_{bj} = \sum_{ij} A^i_{mi}B^j_{nj} \quad (6)$$

$$mi = \frac{N\left(B^i - A^i\right)a_i}{N_{CAi}} \quad (7)$$

$$nj = \frac{N\left(B^j - A^j\right)b_j}{N_{CBj}} \quad (8)$$

where N_{CAi} and N_{CBj} represent the nearest total coordination numbers of the A^i and B^j ions in the crystal. $N(B^j–A^j)$ represents the nearest coordination number contributed by the A^i ion, and $N(A^j–B^j)$ represents the nearest coordination number contributed by the B^j ion. According to the atomic coordination number and occupancy, the complex crystal of CMO could be decomposed as follows:

$$\begin{aligned}
&Ce_2(MoO_4)_2(Mo_2O_7)\\
&= Ce(1)Ce(2)Mo(1)Mo(2)Mo(3)Mo(4)O(1)O(2)O(3)O(4)O(5)O(6)O(7)O(8)\\
&O(9)O(10)O(11)O(12)O(13)O(14)O(15)\\
&= Ce(1)_{1/7}O(3)_{1/2}+Ce(1)_{1/7}O(4)_{1/3}+Ce(1)_{1/7}O(5)_{1/2}+Ce(1)_{1/7}O(6)_{1/2}+Ce(1)_{1/7}O(8)_{1/3}\\
&+Ce(1)_{1/7}O(11)_{1/3}+Ce(1)_{1/7}O(15)_{1/3}\\
&+Ce(2)_{1/8}O(1)_{1/2}+Ce(2)_{1/8}O(2)_{1/2}+Ce(2)_{1/8}O(4)_{1/3}+Ce(2)_{1/8}O(7)_{1/2}+Ce(2)_{1/8}O(8)_{1/3}\\
&+Ce(2)_{1/8}O(10)_{1/2}+Ce(2)_{1/8}O(11)_{1/3}+Ce(2)_{1/8}O(14)_{1/2}\\
&+Mo(1)_{1/4}O(1)_{1/2}+Mo(1)_{1/4}O(2)_{1/2}+Mo(1)_{1/4}O(3)_{1/2}+Mo(1)_{1/4}O(4)_{1/3}\\
&+Mo(2)_{1/4}O(5)_{1/2}+Mo(2)_{1/4}O(6)_{1/2}+Mo(2)_{1/4}O(7)_{1/2}+Mo(2)_{1/4}O(8)_{1/3}\\
&+Mo(3)_{1/4}O(9)_{1/2}+Mo(3)_{1/4}O(10)_{1/2}+Mo(3)_{1/4}O(11)_{1/3}+Mo(3)_{1/4}O(12)_{1/2}\\
&+Mo(4)_{1/6}O(9)_{1/2}+Mo(4)_{1/6}O(12)_{1/2}+Mo(4)_{1/6}O(13)+Mo(4)_{1/6}O(14)_{1/2}\\
&+Mo(4)_{1/3}O(15)_{2/3}
\end{aligned} \quad (9)$$

Table 3
Bond length (d), bond ionicity (f_i), lattice energy (U), bond energy (E), and thermal-expansion coefficient (α) of $Ce_2(MoO_4)_2(Mo_2O_7)$ ceramics.

Bond type	d (Å)	f_i (%)	U (kJ/mol)	E (kJ/mol)	α (10^{-6}/K)
Ce(1)–O(3) × 1	2.3854	65.66	806	430.87	6.4004
Ce(1)–O(4) × 1	2.4959	86.74	802	411.79	7.5167
Ce(1)–O(5) × 1	2.4189	65.87	797	424.90	6.5085
Ce(1)–O(6) × 1	2.4458	66.03	790	420.23	6.5942
Ce(1)–O(8) × 1	2.4779	86.69	807	414.78	7.4505
Ce(1)–O(11) × 1	2.6177	71.43	791	392.63	7.6653
Ce(1)–O(15) × 1	2.3601	86.31	839	435.48	7.0455
Ce(2)–O(1) × 1	2.4417	70.64	671	420.93	8.0064
Ce(2)–O(2) × 1	2.4443	70.66	671	420.48	8.0064
Ce(2)–O(4) × 1	2.4973	89.42	676	411.56	9.0329
Ce(2)–O(7) × 1	2.4044	70.41	680	427.46	7.8584
Ce(2)–O(8) × 1	2.5046	89.44	673	410.36	9.0873
Ce(2)–O(10) × 1	2.4236	70.53	675	424.07	7.9401
Ce(2)–O(11) × 1	2.7495	90.00	624	373.81	10.0497
Ce(2)–O(14) × 1	2.4756	70.84	663	415.17	8.1412
Mo(1)–O(1) × 1	1.7415	90.09	7480	593.07	−0.4850
Mo(1)–O(2) × 1	1.7514	90.12	7451	589.72	−0.4746
Mo(1)–O(3) × 1	1.7541	90.12	7443	588.81	−0.4717
Mo(1)–O(4) × 1	1.8103	78.10	8114	570.53	−0.2824
Mo(2)–O(5) × 1	1.7380	90.08	7491	594.26	−0.4890
Mo(2)–O(6) × 1	1.7489	90.11	7458	590.56	−0.4771
Mo(2)–O(7) × 1	1.7525	90.12	7447	589.35	−0.4731
Mo(2)–O(8) × 1	1.8075	78.08	8123	571.41	−0.2856
Mo(3)–O(9) × 1	1.7280	90.05	7521	597.70	−0.4996
Mo(3)–O(10) × 1	1.7543	90.12	7442	588.74	−0.4713
Mo(3)–O(11) × 1	1.7578	77.83	8281	587.57	−0.3406
Mo(3)–O(12) × 1	1.8283	90.31	7227	564.91	−0.3911
Mo(4)–O(9) × 1	2.4186	76.93	3484	427.04	1.9527
Mo(4)–O(12) × 1	1.9418	75.05	4120	531.89	1.1621
Mo(4)–O(13) × 1	1.6780	46.08	4277	615.51	0.4817
Mo(4)–O(14) × 1	1.7626	73.87	4421	585.97	0.8673
Mo(4)–O(15)^1 × 1	1.9149	90.41	4658	539.37	1.1407
Mo(4)–O(15)^2 × 1	2.0773	90.80	4386	497.20	1.4080

In the CMO system, the effective valence electron number of Ce and Mo cations were $Z_{Ce} = 3$ and $Z_{Mo} = 6$, and it differed in O anion, for instance, $Z_O = 6/7$ in Ce(1)–O(3) bond, $Z_O = 3/4$ in Ce(2)–O(1) bond, and $Z_O = 3$ in Mo(1)–O(1) bond. Furthermore, ε_r could be evaluated by bond ionicity, and the inherent connection could be found in Eq. (10) [30].

$$\varepsilon_r = \frac{n^2 - 1}{1 - f_i} + 1 \tag{10}$$

where n is the refractive index. The bond ionicity (f_i) could be evaluated using Eqs. (11)–(15) [30–33].

$$f_i^{\mu} = \frac{(C^{\mu})^2}{\left(E_g^{\mu}\right)^2} = \frac{(C^{\mu})^2}{(E_h^{\mu})^2 + (C^{\mu})^2} \tag{11}$$

$$(E_h^{\mu})^2 = \frac{39.74}{(d^{\mu})^{2.48}} \tag{12}$$

$$C^{\mu} = 14.4 b^{\mu} exp\left(-k_s^{\mu} r_0^{\mu}\right)\left[\frac{(Z_A^{\mu})^*}{r_0^{\mu}} - (n/m)\frac{(Z_B^{\mu})^*}{r_0^{\mu}}\right] \tag{13}$$

$$k_s^{\mu} = (4k_F/\pi a_B)^{1/2} \tag{14}$$

$$r_0^{\mu} = \frac{1}{2} d^{\mu} \tag{15}$$

where E_h^{μ} and C^{μ} denote the homopolar and heteropolar parts of the average energy gap, respectively. d^{μ} is the bond length of an individual bond μ. $(Z_A^{\mu})^*$ and $(Z_B^{\mu})^*$ are the effective number of valence electrons on the cation A and the anion B, respectively. Moreover, $exp(-k_s^{\mu} r_0^{\mu})$ is the Thomas–Fermi screening factor, where α_B is the Bohr radius. The f_i of the

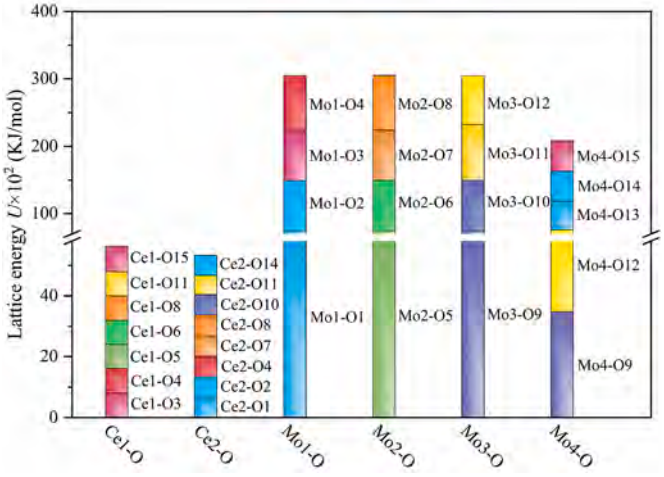

Fig. 7. Comparison of lattice energy (U) between different bonds in $Ce_2(MoO_4)_2(Mo_2O_7)$ ceramics.

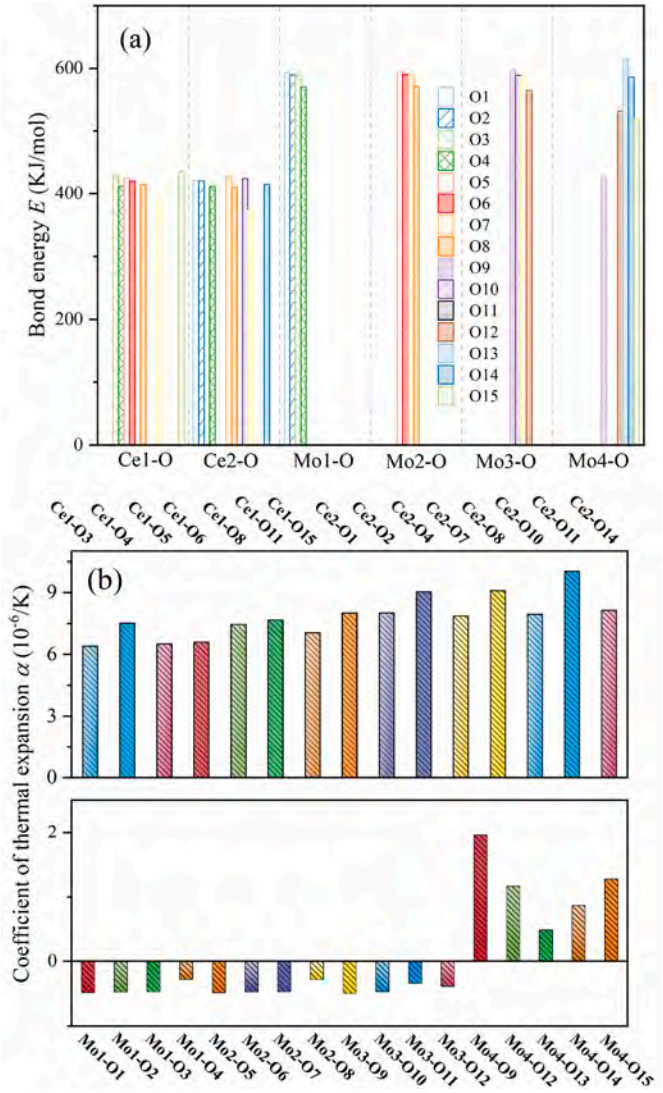

Fig. 8. (a) Bond energy (E) and (b) thermal-expansion coefficient (α) of $Ce_2(MoO_4)_2(Mo_2O_7)$ ceramics.

Table 4
Character table of irreducible representations and the classification of Infrared and Raman active modes of $Ce_2(MoO_4)_2(Mo_2O_7)$.

$C_i(-1)$	C_1	i	Selection rules
$A_g\Gamma_1^+$	1	1	α_{xx}, α_{yy}, α_{zz}, α_{xy}, α_{xz}, α_{yz}, R_x, R_y, R_z
$A_u\Gamma_1^-$	1	−1	T_x, T_y, T_z

$\Gamma_{optic} = 63A_g + 60A_u$.
Raman active modes: 63 A_g.
Infrared active modes: $60A_u$.

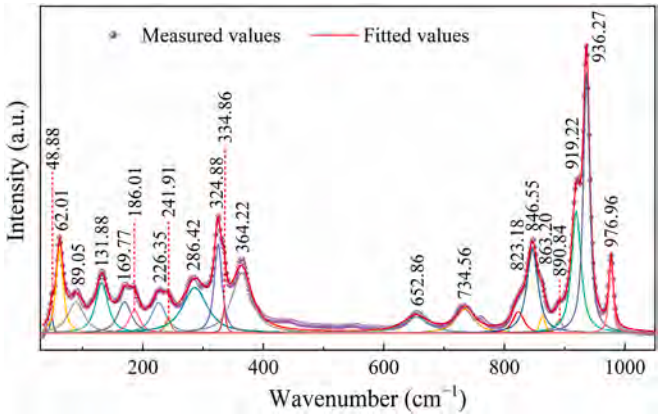

Fig. 9. Measured and fitted Raman spectra and the extracted frequency of all peaks.

CMO ceramics is presented in Fig. 6, and the values are listed in Table 3. The f_i of Mo–O bonds was slightly higher than that of Ce–O bonds (Af_i (Mo–O) = 83.24%; Af_i (Ce–O) = 76.71%). This result suggested that the Mo–O bond made the dominant contribution to ε_r.

The lattice energy is associated with the crystal stability. Therefore, the lattice energy (U) of the CMO ceramics was studied and described via Eqs. (16)–(18) [28,34].

$$U = \sum_{\mu}\left(U_{bi}^{\mu} + U_{bc}^{\mu}\right) \tag{16}$$

$$U_{bi}^{\mu} = 1270\frac{(m+n)Z_{+}^{\mu}Z_{-}^{\mu}}{d^{\mu}}\left(1-\frac{0.4}{d^{\mu}}\right)f_i^{\mu} \tag{17}$$

$$U_{bc}^{\mu} = 2100m\frac{\left(Z_{+}^{\mu}\right)^{1.64}}{\left(d^{\mu}\right)^{0.75}}f_c^{\mu} \tag{18}$$

where Z_{+}^{μ} and Z_{-}^{μ} represent the valence states of the cation and anion which constituted binary crystal, respectively. As shown in Fig. 7, the lattice energy of the Ce(1)–O, Ce(2)–O, Mo(1)–O, Mo(2)–O, Mo(3)–O, and Mo(4)–O bonds were 5,632, 5,333, 30,488, 30,519, 30,471, and 25,346 kJ/mol, respectively. Obviously, U(Mo(n)–O (n = 1, 2, 3, 4)) was higher than U(Ce(m)–O (m = 1, 2)), and which could be inferred that the Mo–O bond provided the main contribution in effecting dielectric loss.

As we all know, a higher bond energy corresponds to the proximity of the τ_f value to zero. Hence, the bond energy (E) was described by Eqs. (19)–(21) [35].

$$E_b^{\mu} = t_c E_c^{\mu} + t_i E_i^{\mu} \tag{19}$$

$$E_i^{\mu} = \frac{332}{d^{\mu}} \tag{20}$$

$$E_c^{\mu} = \frac{(r_{cA}+r_{cB})}{d^{\mu}}\left(E_{A-A}E_{B-B}\right)^{1/2} \tag{21}$$

where t_i and t_c are ionic and covalent proportional coefficient of an individual bond μ. r_{cA} and r_{cB} are the covalent radii of atom A and atom B, respectively. E_{A-A} and E_{B-B} could be obtained from handbook [36]. Besides, the τ_f was negatively related to the coefficients of thermal expansion (α), which can be obtained via Eqs. (22)–(25) [28,31].

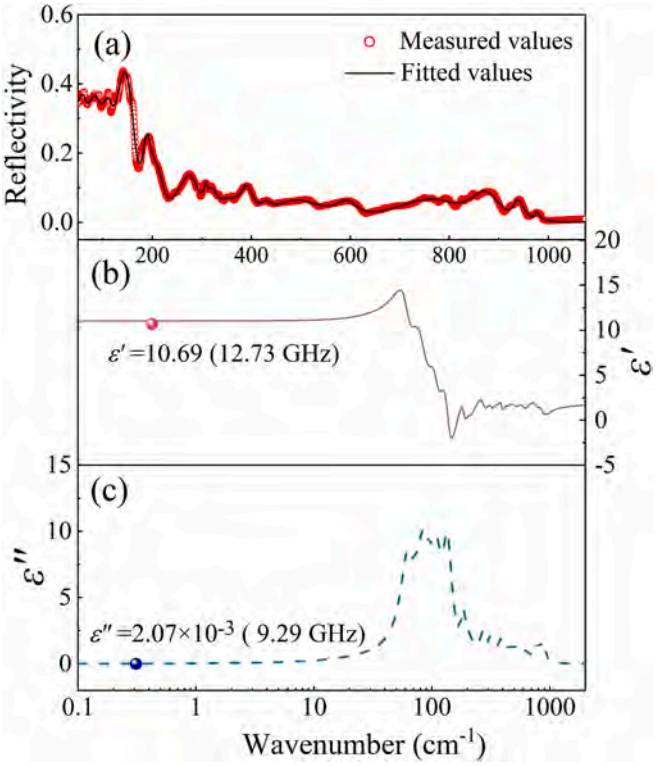

Fig. 10. (a) Measured and fitted infrared reflection spectra, (b) the real parts of the calculated and measured complex permittivity, and (c) the imaginary parts of the calculated and measured complex permittivity for the $Ce_2(MoO_4)_2(Mo_2O_7)$ ceramics sintered at 700 °C.

$$\alpha = \sum_{\mu}F_{mn}^{\mu}\alpha_{mn}^{\mu} \tag{22}$$

$$\alpha_{mn}^{\mu} = -3.1685 + 0.8376\gamma_{mn} \tag{23}$$

$$\gamma_{mn} = \frac{kZ_A^{\mu}N_{CA}^{\mu}}{U_b^{\mu}\Delta_A}\cdot\beta_{mn} \tag{24}$$

$$\beta_{mn} = \frac{m(m+n)}{2n} \tag{25}$$

where F_{mn}^{μ} is the ratio of the bond in total bonds, k is the Boltzmann constant. The sequence of E (Mo(n)–O) > E (Ce(m)–O) could be observed in Fig. 8(a), indicating that the Mo–O bond exerted the dominant influence on τ_f. As shown in Fig. 8(b), most Mo–O bonds possessed a negative value, which exerted a positive influence on τ_f. Based on the above results, the Mo–O bond played a vital role in controlling intrinsic dielectric properties.

Raman spectra is a valid method to estimate the crystal structure evolution, phase composition, and structure–property relationship. Based on the group theory and the symmetry analysis using the Bilbao Crystallographic Server, CMO crystallized in the point group C_i (−1) and classification of the normal modes at the Brillouin zone–center as: Γ_{optic} = $63A_g$+$60A_u$. The irreducible representations containing the selection rule and the classification of Infrared and Raman active modes are listed in Table 4. Notably, the selection rules of T and α represent the molecular translational vibration mode and rotational vibration mode, respectively, which means that T is infrared activated mode and α is Raman activated mode.

Table 5
Phonon parameters obtained from the fitting of $Ce_2(MoO_4)_2(Mo_2O_7)$ ceramics' infrared-reflectivity spectra.

j	ω_{oj} (cm^{-1})	ω_{pj} (cm^{-1})	γ_j (cm^{-1})	$\Delta\varepsilon_j$	tan $\delta_j \times 10^4$
1	61.61	76.10	17.96	1.526	2.02753
2	85.65	146.40	32.79	2.922	3.66868
3	109.54	122.24	26.02	1.254	0.75876
4	136.37	179.06	29.88	1.724	0.77808
5	185.99	94.87	19.36	0.260	0.04090
6	207.87	94.01	37.19	0.205	0.04945
7	273.67	161.11	46.91	0.347	0.06097
8	307.19	36.07	6.83	0.014	0.00028
9	320.09	84.01	26.02	0.069	0.00491
10	353.94	111.90	53.79	0.100	0.01206
11	389.94	121.85	30.37	0.098	0.00548
12	431.09	71.47	29.73	0.027	0.00124
13	501.89	266.40	131.07	0.282	0.04118
14	595.55	158.14	54.87	0.071	0.00306
15	764.85	359.52	143.57	0.221	0.01523
16	863.68	262.17	72.82	0.092	0.00253
17	933.85	110.90	24.36	0.014	0.00011
18	974.23	55.01	11.95	0.003	0.00001
ε_∞				1.81	0
$\sum$				11.029	7.47035

Fig. 9 shows the Raman spectra with all fitted peaks. Because of overlapping features or the intensity of weak modes below the detection limit in Raman spectra, only qualitative analysis of the spectrum was implemented. The spectrum of CMO ceramic has a broad gap between low wavenumber and high wavenumber modes and the intensive line in measured spectral range were also observed. Compared to several similar MoO_4 tetrahedra in varies molybdenum oxide-based ceramics, the Raman modes in the ranges 900−1050 cm^{-1}, 750–900 cm^{-1}, 320–400 cm^{-1} and 280–320 cm^{-1} can be identified as internal symmetric stretching, asymmetric stretching, asymmetric bending and symmetric bending vibrations of the MoO_4 tetrahedra [37–40]. Furthermore, the MoO_6 octahedra give rise to stretching vibrations in the 500–750 cm^{-1} [39]. The Raman peaks below 280 cm^{-1} correspond to a lattice-mode region, an unambiguous assignment of these bands is not possible [39,40].

IRRS were collected to analyse the intrinsic response of dielectric properties. The IR active modes can be represented as $\Gamma_{IR} = 60A_u$. According to the Lorentzian model ((Eq. (26)) and Fresnel's formulas (Eq. (27)) [41], the fitting IRRS is shown in Fig. 10(a). Good agreement was observed by fitting 18 infrared vibrational modes, and the phonon parameters are shown in Table 5. The deviation of the number of IR vibrational modes may be related to overlay and degeneracy.

$$\varepsilon^*(\omega) = \varepsilon_\infty + \sum_{j=1}^{n} \frac{{\omega_{pj}}^2}{{\omega_{oj}}^2 - \omega^2 - j\gamma_j\omega} \tag{26}$$

$$R(\omega) = \left|\frac{1-\sqrt{\varepsilon^*(\omega)}}{1+\sqrt{\varepsilon^*(\omega)}}\right|^2 \tag{27}$$

where $\varepsilon^*(\omega)$ represents the complex dielectric function. ε_∞ is permittivity from the electronic polarisation, ω_{oj} is transverse frequency, ω_{pj} is plasma frequency, and γ_j is the damping factor.

Fig. 10(b) shows the real part of the calculated and measured dielectric constant, and the measured dielectric constant (10.69) was close to the calculated one (12.03). The slight deviation may be due to extrinsic defects such as porosity. The contribution of ε_∞ was 16.4%, indicating that the polarisation contribution primarily originated from ionic polarisation instead of electronic polarisation. Moreover, the primary polarisation contribution was provided by the five vibration modes (j = 1, 2, 3, 4, 5) and was less than 300 cm^{-1} (ε_{1-5} = 69.6%). The dielectric loss (tan δ) could be estimated by Eq. (9).

$$tan\delta = \sum_{j=1}^{n} tan\delta_j = \frac{\varepsilon''}{\varepsilon'} = \frac{\sum_{j=1}^{n} \Delta\varepsilon_j(\gamma_j\omega)\Big/\omega_{oj}^2}{\varepsilon_\infty + \sum_{j=1}^{n}\Delta\varepsilon_j} \tag{28}$$

The imaginary parts of the calculated and measured complex permittivity are illustrated in Fig. 10(c). Table 4 shows that 97.4% of dielectric loss was provided by the five modes (j = 1, 2, 3, 4, 5). Meanwhile, the calculated dielectric loss (tan $\delta = 7.47 \times 10^{-4}$) was close to the measured one (tan $\delta = 1.88 \times 10^{-4}$), indicating that the dielectric properties of CMO ceramic was primarily caused by phonon absorption within the IR range.

4. Conclusion

Novel CMO ceramics were prepared by a conventional solid-state method. Single-phase CMO ceramics belonging to the triclinic system with $P\bar{1}(2)$ space groups were formed. The three-dimensional structure of the CMO structure was connected by [CeO_7], [CeO_8], [MoO_4], and [MoO_6] polyhedra. The optimum microwave dielectric properties were achieved at 700 °C for CMO ceramics: $\varepsilon_r = 10.69$, $Q{\cdot}f = 49{,}440$ GHz (@ 9.29 GHz), and $\tau_f = -30.4$ ppm/°C, it will be a good candidate for dielectric substrates. Based on the chemical bond theory, the Mo–O bond played a significant role in controlling dielectric properties. IRRS analysis was applied to further understand the intrinsic dielectric properties, which were found to be primarily caused by phonon absorption.

Declaration of competing interest

The authors declare that they have no known competing financial interests or personal relationships that could have appeared to influence the work reported in this paper.

Acknowledgments

The authors acknowledge financial supports from National Natural Science Foundation (No. 51972143). The authors are also thankful to the administrators in IR beamline workstation of National Synchrotron Radiation Laboratory (NSRL) for the help in IR measurement.

References

[1] H.H. Guo, M.S. Fu, D. Zhou, C. Du, P.J. Wang, L.X. Pang, W.F. Liu, A.S.B. Sombra, J.Z. Su, Design of a high-efficiency and -gain antenna using novel low-loss, temperature-stable $Li_2Ti_{1-x}(Cu_{1/3}Nb_{2/3})_xO_3$ microwave dielectric ceramics, ACS Appl. Mater. Interfaces 31 (2021) 912–923, https://doi.org/10.1021/acsami.0c18836.
[2] L.X. Pang, D. Zhou, Modification of $NdNbO_4$ microwave dielectric ceramic by Bi substitutions, J. Am. Ceram. Soc. 102 (2019) 2278–2282, https://doi.org/10.1111/jace.16290.
[3] B.J. Tao, W.F. Wang, H.Y. Liu, T.X. Du, H.T. Wu, C.F. Xing, D.Z. Wang, Y.P. Zhang, Low-temperature sintering LiF-doped $Li_4Mg_3[Ti_{0.6}(Mg_{1/3}Nb_{2/3})_{0.4}]_2O_9$ microwave dielectric ceramics for LTCC applications, Ceram. Int. 47 (2021) 2584–2590, https://doi.org/10.1016/j.ceramint.2020.09.104.
[4] C.Z. Yin, Z.Z. Yu, L.L. Shu, L.J. Liu, Y. Chen, C.C. Li, A low-firing melilite ceramic $Ba_2CuGe_2O_7$ and compositional modulation on microwave dielectric properties through Mg substitution, J. Adv. Ceram. 10 (2020) 108–119, https://doi.org/10.1007/s40145-020-0424-3.
[5] C.J. Pei, J.J. Tan, Y. Li, G.G. Yao, Y.M. Jia, R.Z. Yu, P. Liu, H.W. Zhang, Effect of Sb-site nonstoichiometry on the structure and microwave dielectric properties of $Li_3Mg_2Sb_{1-x}O_6$ ceramics, J. Adv. Ceram. 9 (2020) 588–594, https://doi.org/10.1007/s40145-020-0397-2.
[6] M.T. Sebastian, H. Wang, H.L. Jantunen, Low temperature co-fired ceramics with ultra-low sintering temperature: a review, Curr. Opin. Solid St. M. 20 (2016) 151–170, https://doi.org/10.1016/j.cossms.2016.02.004.
[7] S.Z. Hao, D. Zhou, L.X. Pang, The spectra analysis and microwave dielectric properties of $[Ca_{0.55}(Sm_{1-x}Bi_x)_{0.3}]MoO_4$ ceramics, J. Am. Ceram. Soc. 102 (2019) 3103–3109, https://doi.org/10.1111/jace.16339.
[8] H.H. Guo, D. Zhou, L.X. Pang, Z.M. Qi, Microwave dielectric properties of low firing temperature stable scheelite structured (Ca, Bi)(Mo, V)O_4 solid solution ceramics for LTCC applications, J. Eur. Ceram. Soc. 39 (2019) 2365–2373, https://doi.org/10.1016/j.jeurceramsoc.2019.02.010.

[9] B.J. Tao, C.F. Xing, W.F. Wang, H.T. Wu, Y.Y. Zhou, A novel $Ce_2Zr_3(MoO_4)_9$ microwave dielectric ceramic with ultra-low firing temperature, Ceram. Int. 45 (2019) 24675–24683, https://doi.org/10.1016/j.ceramint.2019.08.206.
[10] Y.H. Zhang, J.J. Sun, N. Dai, Z.C. Wu, H.T. Wu, C.H. Yang, Crystal structure, infrared spectra and microwave dielectric properties of novel extra low-temperature fired $Eu_2Zr_3(MoO_4)_9$ ceramics, J. Eur. Ceram. Soc. 39 (2019) 1127–1131, https://doi.org/10.1016/j.jeurceramsoc.2018.12.042.
[11] J.J. Zheng, C.F. Xing, Y.K. Yang, S.X. Li, H.T. Wu, Z.H. Wang, Structure, infrared reflectivity spectra and microwave dielectric properties of a low-firing microwave dielectric ceramic $Pr_2Zr_3(MoO_4)_9$, J. Alloys Compd. 826 (2020) 153893, https://doi.org/10.1016/j.jallcom.2020.153893.
[12] Y.H. Zhang, H.T. Wu, Crystal structure and microwave dielectric properties of $La_2(Zr_{1-x}Ti_x)_3(MoO_4)_9$ ($0 \leq x \leq 0.1$) ceramics, J. Am. Ceram. Soc. 102 (2019) 4092–4102, https://doi.org/10.1111/jace.16268.
[13] J.J. Zheng, Y.H. Liu, B.J. Tao, Q. Zhang, H.T. Wu, X.Y. Zhang, Crystal structure and optimised microwave dielectric properties of $Ce_2(Zr_{1-x}Ti_x)_3(MoO_4)_9$ solid solutions, Ceram. Int. 47 (2021) 5624–5630, https://doi.org/10.1016/j.ceramint.2020.10.147.
[14] D. Zhou, W.B. Li, L.X. Pang, J. Guo, Z.M. Qi, T. Shao, Z.X. Yue, X. Yao, Sintering behavior and dielectric properties of ultra-low temperature fired silver molybdate ceramics, J. Am. Ceram. Soc. 97 (2014) 3597–3601, https://doi.org/10.1111/jace.13159.
[15] G.D. Fallon, B.M. Gatehouse, The Crystal Structure of a Complex Cerium (III) molybdate containing a dimolybdate chain, $Ce_2(MoO_4)_2(Mo_2O_7)$, J. Solid State Chem. 44 (1982) 156–161, https://doi.org/10.1016/0022-4596(82)90360-7.
[16] B.W. Hakki, P.D. Coleman, A dielectric resonator method of Measuring Inductive capacities in the millimeter range, IRE Trans. Microw. Theory Tech. 8 (1960) 402–410, https://doi.org/10.1109/TMTT.1960.1124749.
[17] W.E. Courtney, Analysis and evaluation of a method of measuring the complex permittivity and permeability microwave insulators, IEEE Trans. Microw. Theor. Tech. 18 (1970) 476–485, https://doi.org/10.1109/TMTT.1970.1127271.
[18] D. Zhao, F.F. Li, Y.M. Yao, C.A. Huan, E.X. Zhao, β-$Nd_2Mo_4O_5$, Acta Crystallogr. E 66 (2010) i85, https://doi.org/10.1107/S1600536810048609.
[19] F.Y. Huang, H. Su, Y.X. Li, H.W. Zhang, X.L. Tang, Low-temperature sintering and microwave dielectric properties of $CaMg_{1-x}Li_{2x}Si_2O_6$ ($x = 0-0.3$) ceramics, J. Adv. Ceram. 9 (2020) 471–480, https://doi.org/10.1007/s40145-020-0390-9.
[20] X. Zhang, Z.X. Fang, H.Y. Yang, P. Zhao, X. Zhang, Y.P. Li, Z. Xiong, H.C. Yang, S. R. Zhang, B. Tang, Lattice evolution, ordering transformation and microwave dielectric properties of rock-salt $Li_{3+x}Mg_{2-2x}Nb_{1-x}Ti_{2x}O_6$ solid-solution system: a newly developed pseudo ternary phase diagram, Acta Mater. 206 (2021) 116636, https://doi.org/10.1016/j.actamat.2021.116636.
[21] X. Zhang, X. Zhang, Z.X. Fang, Z. Xiong, H.Y. Yang, S.R. Zhang, B. Tang, Effects of lattice evolution and ordering on the microwave dielectric properties of tin-modified $Li_3Mg_2NbO_6$-based ceramics, J. Phys. Chem. C 124 (2020) 22069–22081, https://doi.org/10.1021/acs.jpcc.0c04762.
[22] R.D. Shannon, Dielectric polarizabilities of ions in oxides and fluorides, J. Appl. Phys. 73 (1993) 348–366, https://doi.org/10.1063/1.353856.
[23] J.J. Zheng, Y.K. Yang, H.T. Wu, Y.Y. Zhou, Z.L. Zhang, Structure, infrared spectra and microwave dielectric properties of the novel Eu_2TiO_5 ceramics, J. Am. Ceram. Soc. 103 (2020) 4333–4341, https://doi.org/10.1111/jace.17092.
[24] H.Y. Yang, S.R. Zhang, Y.W. Chen, H.C. Yang, Y. Yuan, E.Z. Li, Crystal chemistry, Raman spectra, and bond characteristics of trirutile-type $Co_{0.5}Ti_{0.5}TaO_4$ microwave dielectric ceramics, Inorg. Chem. 58 (2019) 968–976, https://doi.org/10.1021/acs.inorgchem.8b03169.
[25] D. Zhou, J. Li, L.X. Pang, G.H. Chen, Z.M. Qi, D.W. Wang, I.M. Reaney, Crystal structure, infrared spectra, and microwave dielectric properties of temperature-stable zircon-type (Y, Bi)VO_4 solid-solution ceramics, ACS Omega 1 (2016) 963–970, https://doi.org/10.1021/acsomega.6b00274.
[26] N. Ichinose, T. Shimada, Effect of grain size and secondary phase on microwave dielectric properties of $Ba(Mg_{1/3}Ta_{2/3})O_3$ and $Ba([Mg, Zn]_{1/3}Ta_{2/3})O_3$ systems, J. Eur. Ceram. Soc. 26 (2006) 1755–1759, https://doi.org/10.1016/j.jeurceramsoc.2005.09.032.
[27] C.F. Tseng, Microwave dielectric properties of low loss microwave dielectric ceramics: $a_{0.5}Ti_{0.5}NbO_4$ (A=Zn, Co), J. Eur. Ceram. Soc. 34 (2014) 3641–3648, https://doi.org/10.1016/j.jeurceramsoc.2014.06.010.
[28] H.Y. Yang, S.R. Zhang, H.C. Yang, E.Z. Li, Usage of P-V-L bond theory in studying the structural/property regulation of microwave dielectric ceramics: a review, Inorg. Chem. Front. 7 (2020) 4711–4753, https://doi.org/10.1039/D0QI00907E.
[29] Z.J. Wu, Q.B. Meng, S.Y. Zhang, Semiempirical study on the valences of Cu and bond covalency in $Y_{1-x}Ca_xBa_2Cu_3O_{6+y}$, Phys. Rev. B 58 (1998) 958–962, https://doi.org/10.1103/PhysRevB.58.958.
[30] S.S. Batsanov, Dielectric methods of studying the chemical bond and the concept of electronegativity, Russ. Chem. Rev. 51 (1982) 684–697, https://doi.org/10.1070/RC1982v051n07ABEH002900.
[31] X. Zhou, L.T. Liu, J.J. Sun, N.K. Zhang, H.Z. Sun, H.T. Wu, W.H. Tao, Effects of $(Mg_{1/3}Sb_{2/3})^{4+}$ substitution on the structure and microwave dielectric properties of $Ce_2Zr_3(MoO_4)_9$ ceramics, J. Adv. Ceram. 10 (4) (2021) 778–789, https://doi.org/10.1007/s40145-021-0472-3.
[32] B.F. Levine, Bond susceptibilities and ionicities in complex crystal structures, J. Chem. Phys. 59 (1973) 1463–1486, https://doi.org/10.1063/1.1680204.
[33] L.T. Liu, Y.G. Chen, Z.B. Feng, H.T. Wu, X.Y. Zhang, Crystal structure, infrared spectra, and microwave dielectric properties of the $EuNbO_4$ ceramic, Ceram. Int. 47 (2021) 4321–4326, https://doi.org/10.1016/j.ceramint.2020.09.176.
[34] H.C. Yang, S.R. Zhang, H.Y. Yang, Y. Yuan, E.Z. Li, Vibrational spectroscopic and crystal chemical analyses of double perovskite Y_2MgTiO_6 microwave dielectric ceramics, J. Am. Ceram. Soc. 103 (2020) 1121–1130, https://doi.org/10.1111/jace.16737.
[35] J.X. Bi, C.F. Xing, C.H. Yang, H.T. Wu, Phase composition, microstructure and microwave dielectric properties of rock salt structured Li_2ZrO_3–MgO ceramics, J. Eur. Ceram. Soc. 38 (2018) 3840–3846, https://doi.org/10.1016/j.jeurceramsoc.2018.04.034.
[36] Y.R. Luo, Comprehensive Handbook of Chemical Bond Energies, CRC press, Boca Raton, 2007.
[37] H.C. Yang, S.R. Zhang, H.Y. Yang, Y. Yuan, E.Z. Li, $Gd_2Zr_3(MoO_4)_9$ microwave dielectric ceramics with trigonal structure for LTCC application, J. Am. Ceram. Soc. (2019) 1–9, https://doi.org/10.1111/jace.16744, 00.
[38] J. Dhanya, E.K. Suresh, R. Naveenraj, R. Ratheesh, Structure and microwave dielectric properties of low temperature sinterable $NaR_5(MoO_4)_8$ (R = La, Pr, Nd, Sm) ceramics, J. Electron. Mater. 48 (2019) 4040–4049, https://doi.org/10.1007/s11664-019-07165-y.
[39] N.K. James, R. Ratheesh, Microwave dielectric properties of low-temperature sinterable $BaCe_2(MoO_4)_4$ ceramics, J. Am. Ceram. Soc. 93 (2010) 931–933, https://doi.org/10.1111/j.1551-2916.2009.03508.x.
[40] R.F. Shen, B.H. Yuan, S.L. Li, X.H. Ge, J. Guo, E.J. Liang, Near-zero thermal expansion of $Zr_xHf_{1-x}MgMo_3O_{12}$ in a larger temperature range, Optik 165 (2018) 1–6, https://doi.org/10.1016/j.ijleo.2018.03.035.
[41] J. Petzelt, S. Kamba, Submillimetre and infrared response of microwave materials: extrapolation to microwave properties, Mater. Chem. Phys. 79 (2003) 175–180, https://doi.org/10.1016/S0254-0584(02)00269-9.